

SLITTED ACCURACY OF THIN WALLS IN LASER POWDER BED FUSION

B. Johnstone*, C. Saldana*, and K. Saleeby†

* George W. Woodruff School of Mechanical Engineering, Georgia Institute of Technology, Atlanta, GA 30332

† Georgia Institute of Technology Manufacturing Institute, Atlanta, GA 30332

Abstract

Accurate fabrication of detailed features is a critical roadblock for adoption of certified metal additive manufacturing components. However, as features decrease in size, their dimensional accuracy becomes more sensitive to variation in processing conditions including heat input and contact with the recoater blade. In this paper, slitted thin walls were manufactured with varying thicknesses, slit aspect ratios, and laser powers. Error in dimensional accuracy of slits was measured via X-ray computed tomography, stemming from dross formation on overhanging horizontal edges and deflection recoater blade contact on vertical edges. Experimental results indicate slits were more likely to have lower dimensional accuracy on their longer side. Meanwhile, increasing laser power decreased deflection of the vertical edges but increased dross formation on the horizontal edges. Each type of defect was more prominent in thinner walls. Understanding the balance of these conditions will allow greater use of precise geometries for various applications.

Introduction

As metal additive manufacturing (MAM) processes become more widely adopted in a variety of industries, these processes will be used to make unique components with increasingly complex geometries [1]. One such example is using the smaller achievable feature size of laser powder bed fusion (PBF-LB) to manufacture components with thin walls, such as heat exchangers [2], cooling fins [3], and component lightweighting [4]. However, as these components get smaller, they start to become more susceptible to common process defects such as lack of fusion (LoF). Due to the reduced overall area of the parts, typically happening in parts less than 1 mm in thickness, the laser spends less time lasing the parts and therefore imparts less overall energy into the parts [5].

A macro-scale impact from more prevalent LoF defects is the parts are more likely to warp due to contact from the recoater blade. Since the walls have a smaller area alongside the overall lower density due to the LoF defects, thin walls are overall less resistant to external forces than their bulkier counterparts [6]. This means the thin walls can be deformed by the recoater blade contacting the parts, pushing each layer in the recoat direction. Two primary solutions have been shown to reduce this issue. The first solution is to increase energy density and reduce the LoF defects [7]. The second solution is to angle the walls so the thinnest side is perpendicular to the recoat direction [8]. This reduces the contact area between the recoater blade and the part, minimizing the pressure onto that wall that can cause distortion.

As these features are used in more complex components, they will be used alongside other features known to increase certain defects. One very common feature is overhangs, which are known to increase the likelihood of defects such as high surface roughness [9] and warpage [10]. While there have been solutions proposed to alleviate these issues, such decreasing energy density [11] and using support structures [12], these solutions are not always applicable. In the case of thin walls with unsupported overhangs, the walls typically need higher energy density to reduce LoF and recoater-impact defects. Additionally, due to the smaller size of these features, support structures become less practical since they cannot be easily removed without impacting the finished part.

This work seeks to understand how these features interact with each other in the PBF-LB process. A set of walls were printed with different combinations of design and manufacturing parameters. The dimensional

accuracy of the slits was quantified by measuring surface roughness on the top surface and slanting of the side surfaces from scans via X-ray computed tomography. With these measurements, the relationships between design parameters with opposing machine parameter solutions can be quantitatively evaluated.

Methods

2.1 Sample Design and Manufacturing

An *EOS M280* PBF-LB machine was used to manufacture 27 walls with varying combinations of design and manufacturing parameters out of 316L stainless steel ($D50 = 49.9$ microns). The walls were all printed on reduced build volume (RBV) plate of 90 mm x 90 mm. The length and height of each wall was held constant at 10 mm and 5 mm, respectively. For design parameters, each wall had one of three different wall thicknesses (0.38 mm, 0.50 mm, 1.00 mm). These thicknesses were determined because 1.00 mm is typically considered to be the transition thickness where thin-wall behavior begins to appear, while the 0.38 mm limit is just above the threshold where the machine transitions from traditional rastering to single-track. Additionally, each wall had one of three different slit types (horizontal, vertical, no slits [walls without slits were not analyzed in this work]) (Table 1). Slits were all rectangles with dimensions of 1 mm x 2 mm, with the slit aspect ratio (SAR), which is defined as the slit width divided by the slit height, varying to determine if a longer slit height or width had more impact on dimensional accuracy. Horizontal slits (SAR = 2.0) had a width of 2 mm and a height of 1 mm, while the vertical slits (SAR = 0.5) had a width of 1 mm and height of 2 mm (Figure 1). For machine parameters, each wall had one of three different laser powers (114 W, 214 W, 341 W), with 214 W being the standard power for bulk parts. All other machine parameters were held constant (Table 2). To limit the impact of recoater damage to the walls, each wall was oriented with the length of the wall in the recoat direction (Figure 2).

Table 1: Design Parameters

Parameter	Value
Length	10 mm
Height	5 mm
Thickness	0.38 mm, 0.50 mm, 1.00 mm
Slits	Horizontal (2 mm x 1 mm), Vertical (1 mm x 2 mm)

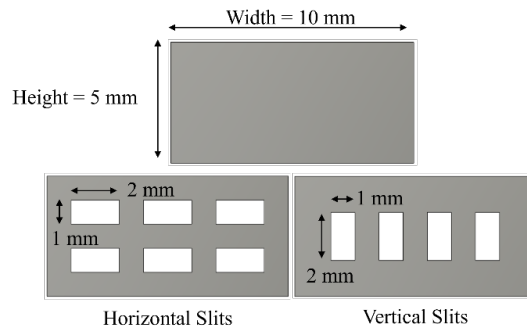


Figure 1: Slit Geometries for No Slits (Top Center), Horizontal Slits (Bottom Left), and Vertical Slits (Bottom Right)

Table 2: Manufacturing Parameters

Parameter	Value
Scan Speed	928.1 mm/s
Hatch Spacing	40 microns
Layer Thickness	40 microns
Laser Power	114 W, 214 W, 314 W

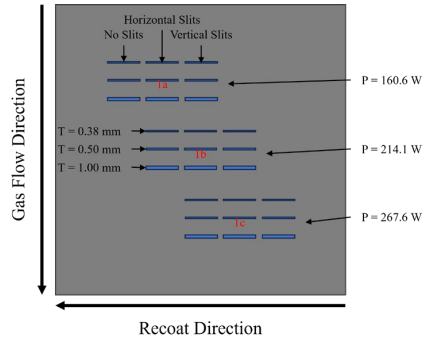


Figure 2: Build Layout

2.2 X-Ray Computed Tomography

After manufacturing, each sample was scanned in a *Zeiss Metrotom 800*. To optimize contrast and resolution, the walls were scanned with parameters in Table 3. With these parameters, a voxel size of 8 microns was achieved. To reconstruct the scans into a 3D structure, a Feldkamp algorithm was used with a Shepp-Logan filter in MATLAB R2024a using custom code developed by the research group. Each sample was scanned using a polymer-printed fixture to ensure the same orientation between scans.

Table 3: XCT Scanning Parameters

Parameter	Value
Voltage	75 kV
Current	80 mA
Projections	1450
Gain	8x

After each sample was scanned, a feature-based registration process was performed. Each 3D structure was converted into a surface using an Otsu threshold for binarization (Figure 3a). Then, points were sampled to determine primary, secondary, and tertiary datum features. This was done by setting a region of interest (ROI) in the shape of a rectangular prism for each datum feature. These ROIs were placed and aligned to the bottom (primary), left (secondary), and front (tertiary) faces (Figure 3b) and sampling points within each of these ROIs on one sample (Figure 3c). For each of these sets of points, a plane of best fit was determined using a least-squares algorithm (Figure 3d). Finally, a rotation matrix was calculated to align the primary datum plane to the +Z-direction, the secondary datum plane to the +X-direction, and the tertiary datum plane to the +Y-direction (Figure 3e). Since the scanning fixture ensured all samples had the same orientation, this rotation matrix was applied to all samples to give the same final orientation.

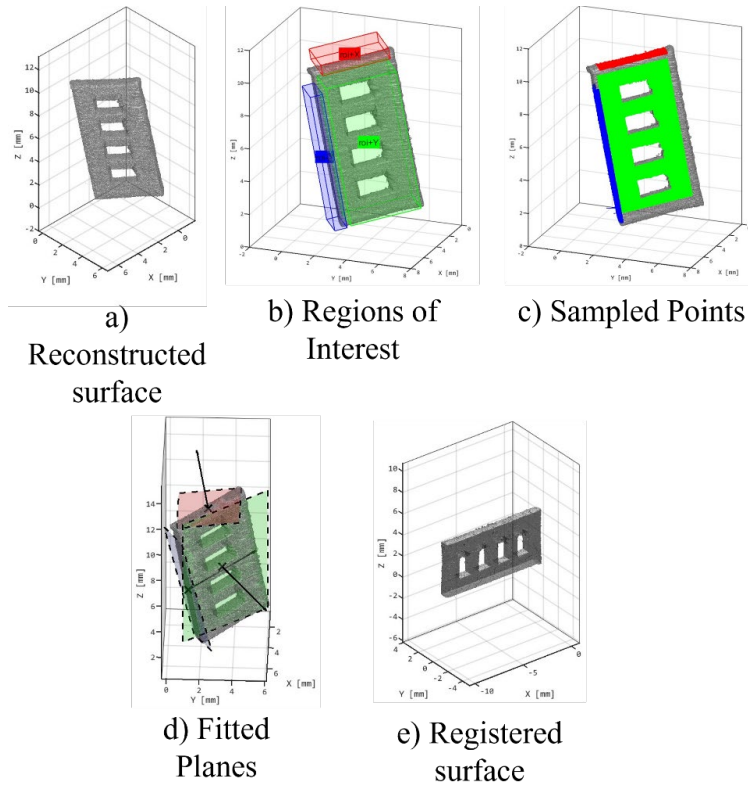


Figure 3: Registration process for sample $T = 1.00$ mm, $SAR = 2$, $P = 314$ W. Process starts with a) reconstructing the surface from the raw XCT scan, b) setting ROI rectangular prisms on each datum face, c) sample points on surface within each ROI, d) determine plane of best fit for each set of sampled points, and e) align each plane normal vector to corresponding coordinate direction.

2.3 Dross Analysis

After each scan was reconstructed into a 3D structure and registered, another ROI in the shape of a rectangular prism was set around each slit. Within each ROI, points on the surface were sampled, and a binary image was created using the X- and Z-coordinates of the sampled points. Then, a boundary finding algorithm was used to find the points along the inner edge of the slit (Figure 4). To distinguish between the top and bottom boundaries, the Z-values of the boundary points were plotted on a histogram. The lower peak corresponded with the bottom boundary while the higher peak corresponded with the top boundary (Figure 5). Points below the bottom boundary line were grouped as bottom boundary points, while points above the top boundary were grouped as top boundary points.

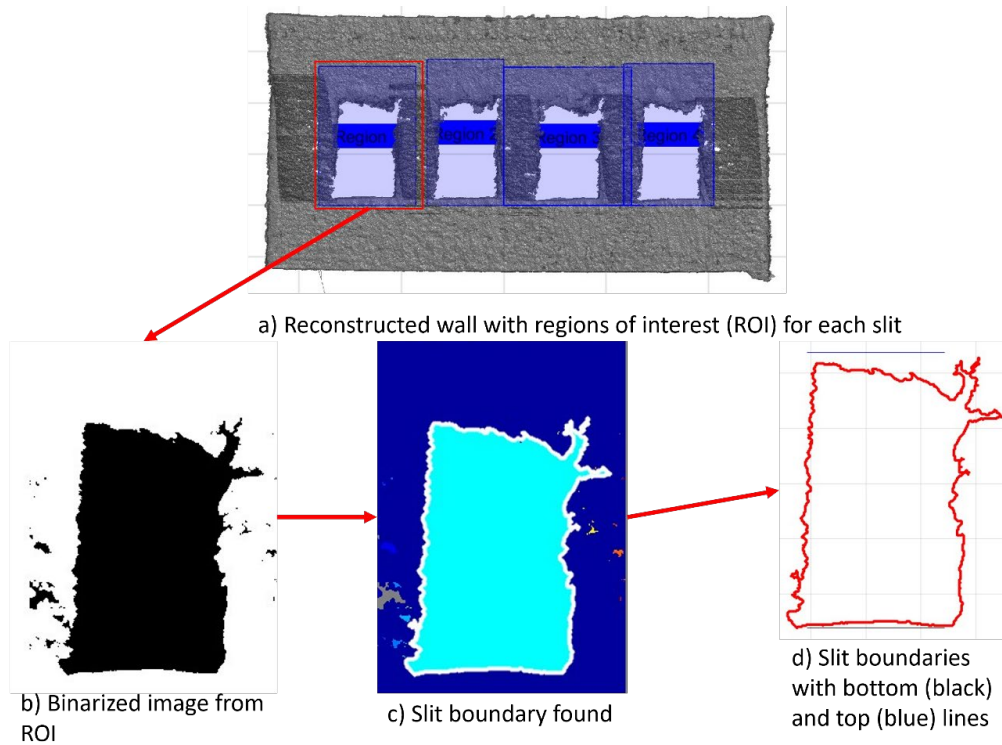


Figure 4: Slit boundary analysis with a) setting ROI on each slit, b) sample points in ROI and use X- and Z-coordinates to create binary image, c) perform boundary finding algorithm to find slit boundaries, and d) plot boundary points.

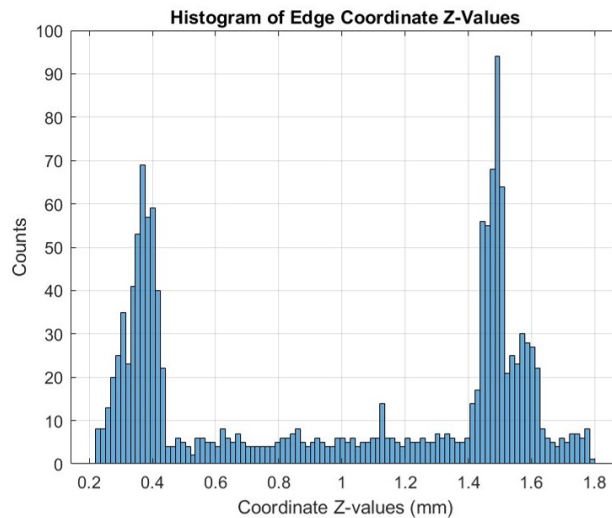


Figure 5: Histogram of Z-coordinate values to find peaks corresponding to top and bottom edges.

Dross was quantified using surface roughness parameters defined in ISO-25178 [13]. These parameters are summarized in Table 4. Points were determined by taking the top boundary line and segmenting points that had a Z-height above the height of 95% of the top boundary line (Figure 6). This top boundary line also served as the datum line for measuring the surface roughness parameters. Points were flipped over the datum line, meaning “peaks” were defined as greater dross formation.

Table 4: Surface Roughness Parameters

Parameter	Symbol	Definition
Maximum Profile Peak Height	Rp	Largest height of peak
Minimum Profile Valley Depth	Rv	Smallest depth of valley
Roughness Average	Ra	Arithmetic mean of ordinate values
Root Mean Squared (RMS) Roughness	Rq	Root mean squared value of ordinate values

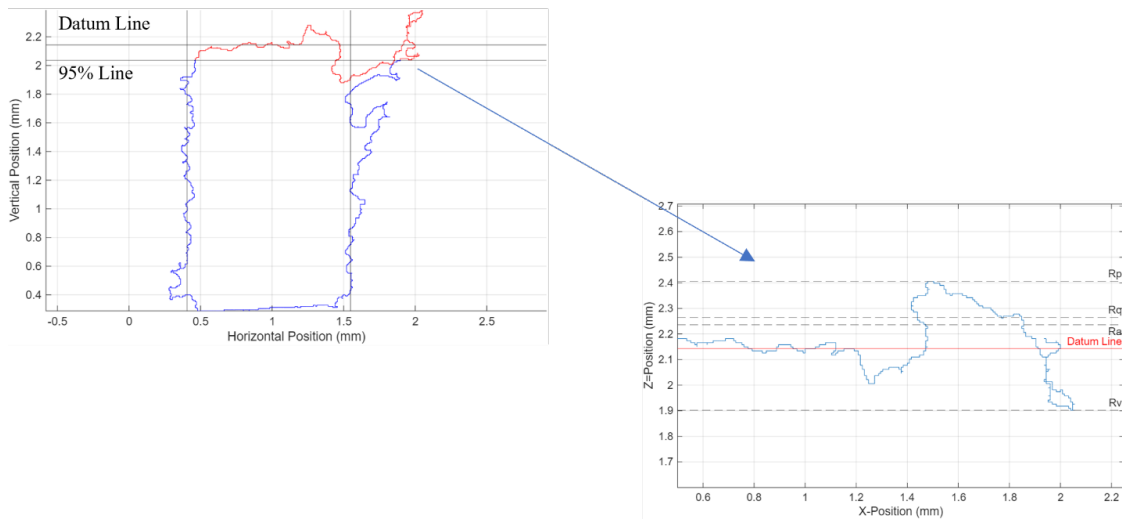


Figure 6: Slit boundary points (blue) plotted with sampled top boundary points (red) plotted with datum and 95% lines shown for reference (left). Those sampled top boundary points were then flipped over the datum line and used to measure surface roughness parameters (right).

2.4 Slanting Analysis

For this work, “slit slanting” (or just slanting) is defined as the angular horizontal deviation of the side walls of each slit. Using the same from the points determined by the ROIs from the dross analysis, side walls were determined by plotting a histogram of the X-coordinates of the edge points (Figure 7). The lower peak corresponded with the left side, while the higher peak corresponded with the right side. For each side, points were sampled as being at least 95% of the distance from the mean line to the corresponding edge line. These points were then plotted with swapped Y- and Z-points, and a line of best fit was calculated using a linear regression algorithm (Figure 8). The slope of this line was used to quantitatively measure slanting, with a larger slope corresponding to greater slanting.

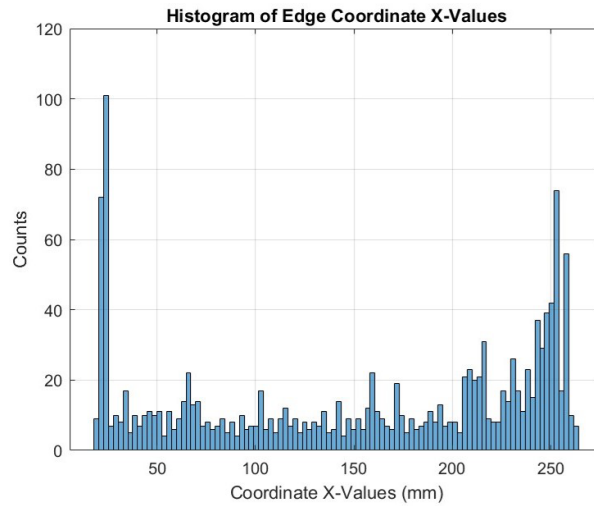


Figure 7: Histogram of X-coordinate values to find peaks corresponding to left and right edges.

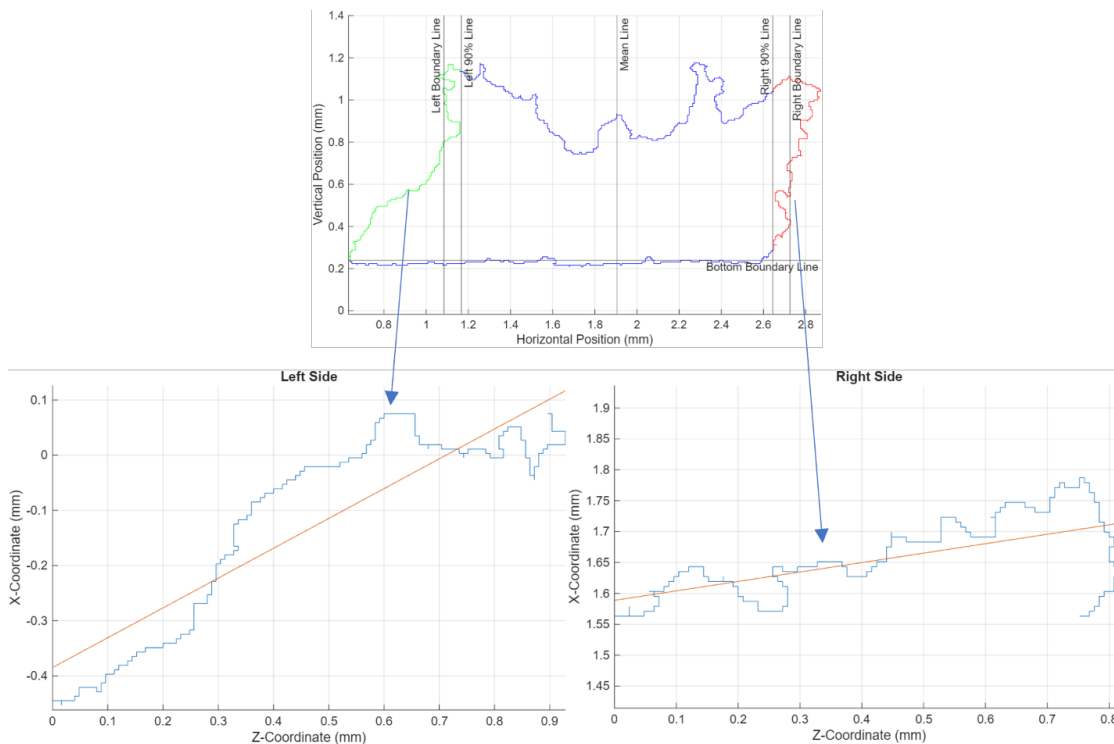


Figure 8: Slit edge points plotted with swapped X- and Z-coordinates (blue) with line of best fit (orange) for both the left and right sides.

Results

3.1 Manufacturing

All samples were successfully manufactured (Figure 9). Observing the samples qualitatively, the lower power samples had more breaks in barriers between slits. This appeared in samples with both horizontal and

vertical slits. In the horizontal slit samples, this resulted in deflections in the gas flow direction, bending the tops of the walls forward. In the vertical slit samples, this resulted in the slit barriers breaking in the recoat direction.

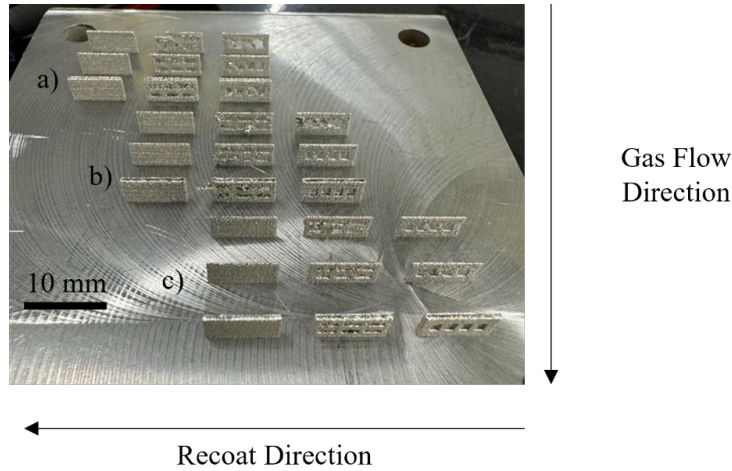


Figure 9: Resultant build with recoat and gas flow directions labeled.

3.2 Dross

Of the three parameters varied in this study, thickness had the smallest impact dross formation (Figure 10). While there are some trends indicating that increasing thickness leads to lower surface roughness, the averages are within 1 standard deviation of each other, indicating the difference is not statistically significant. This is especially true between the 0.38 mm and 0.50 mm samples, which have a difference in averages closer to half a standard deviation or less. The samples with a thickness of 1.00 mm did have a greater difference in surface roughness than the other samples, but again the difference is insignificant.

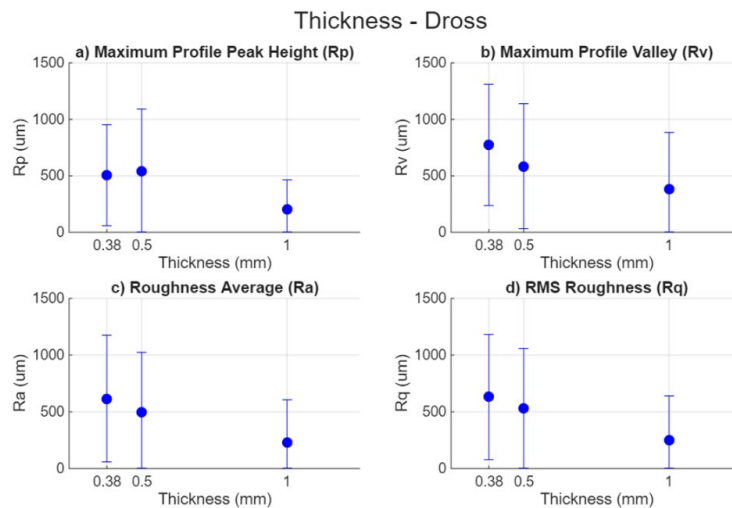


Figure 10: Surface roughness parameters with samples grouped based on designed wall thickness (dashes signify 1 standard deviation).

For the SAR, the difference in dross formation is much clearer (Figure 11). For each surface roughness parameter, the samples with a higher SAR (meaning larger width than height) had a statistically significantly lower value. Additionally, for three of the four parameters (Rp, Ra, and Rq), the distribution of values was similar

between the two SAR values. However, R_v did vary more between the two slit types, being multiple times larger for the slits with a higher SAR.

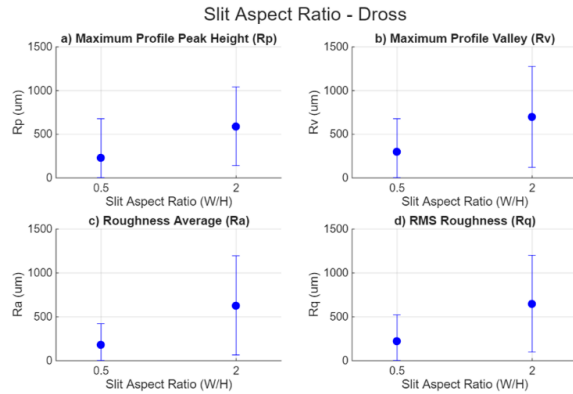


Figure 11: Surface roughness parameters with samples grouped based on slit aspect ratio (dashes signify 1 standard deviation).

For the final parameter, power seems to initially not have a significant impact on dross formation. While the medium power value was slightly different from the other two values, all the averages are within 1 standard deviation of each other.

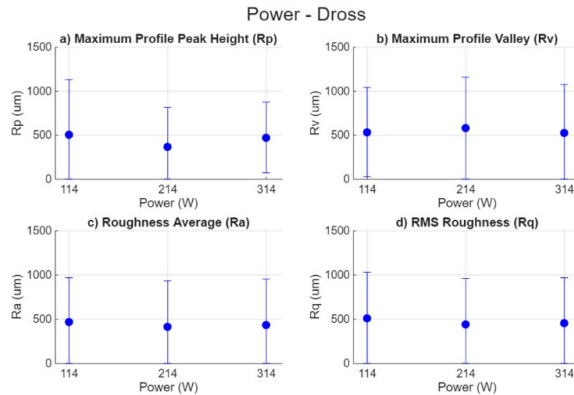


Figure 12: Surface roughness parameters with samples grouped based on laser power (dashes signify 1 standard deviation).

However, when separating the power values based on SAR (Figure 13), a trend appears. For the slits with smaller SAR, increasing power led to a decrease in maximum peak height as well as both average and RMS roughness. This means that with a smaller overhang distance, the increase in power reduced the dross formation. The valley depth, however, displayed a different behavior. While the low and high-power samples had smaller valley depth, the medium power value had a significantly higher valley depth than the others. This, along with the shorter peak height, means that for the medium power, the dross formation was more uniform sections of less dross formation, resulting in low peaks and roughness but large valleys. Meanwhile, for the slits with higher SAR, the difference between samples was once again statistically insignificant. The average roughness values for each parameter were roughly the same, and the standard deviations were large. Therefore, the larger overhang distance results in significant dross formation, regardless of power.

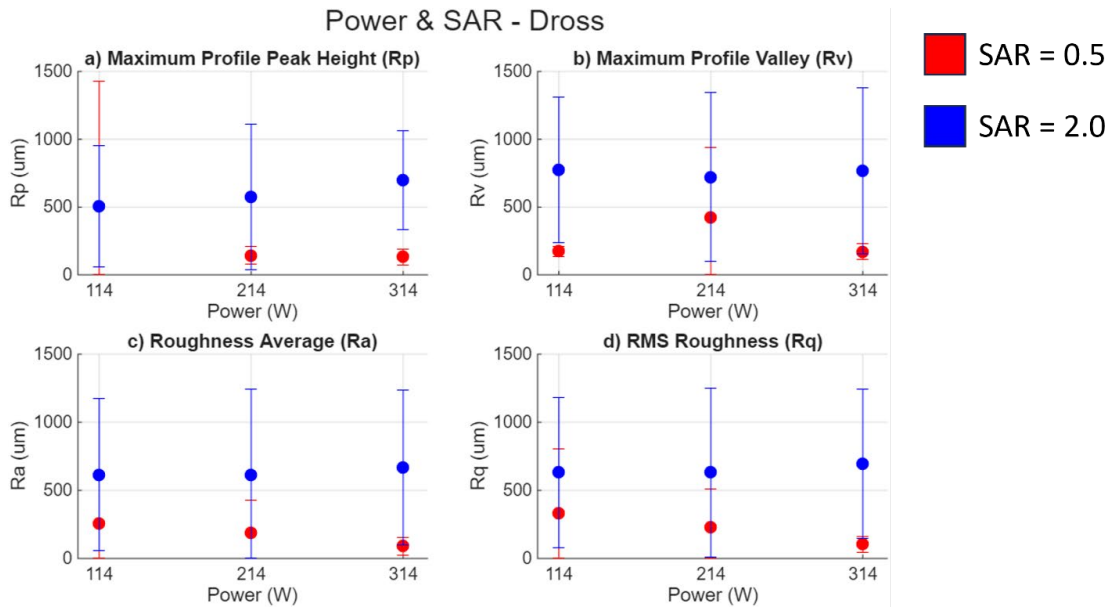


Figure 13: Surface roughness parameters with samples grouped based on laser power and separated by SAR (dashes signify 1 standard deviation).

3.3 Slanting

As with dross formation, wall thickness did not result in significant difference in slanting (Figure 14). While the averages do decrease as wall thickness increased, the decrease was less than 30 microns and are well within 1 standard deviation of the other averages. However, there was a difference in distribution between the 1.00 mm thickness samples and the thinner samples, being roughly half the size.

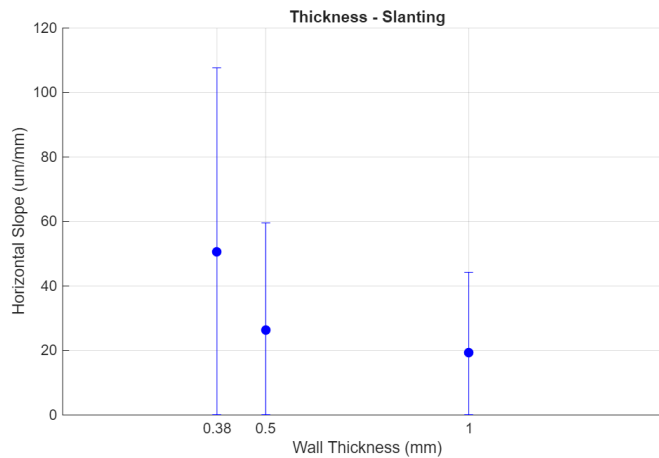


Figure 14: Slanting due to designed wall thickness (dashes signify 1 standard deviation).

SAR had more impact on slanting (Figure 15). The samples with a smaller SAR had a higher average slant and smaller distribution of slants. The samples with higher SAR had a much larger distribution, spanning more than double the range of slants of the samples with lower SAR.

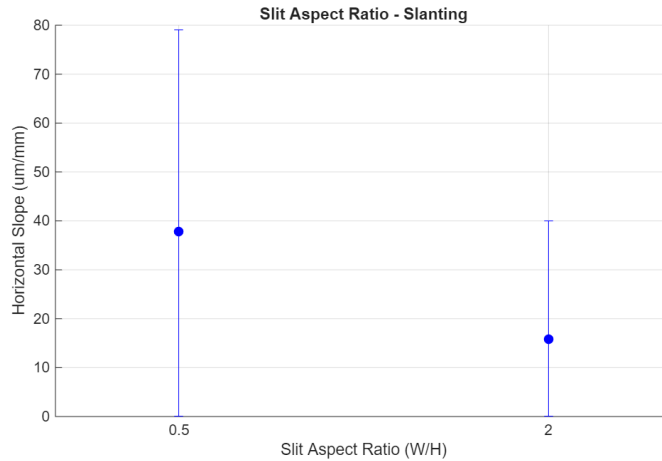


Figure 15: Slanting due to slit aspect ratio (dashes signify 1 standard deviation).

Power also had an impact on slanting, but much smaller than SAR (Figure 16). While the low- and medium-power samples had roughly the same average and distribution of slanting values, the high-power samples had lower average and lower distribution.

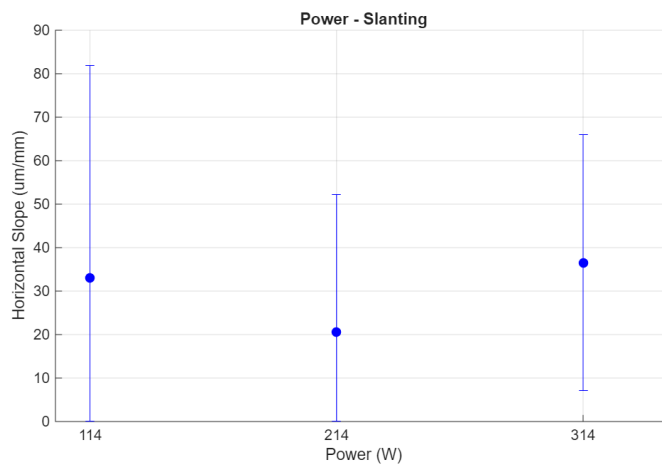


Figure 16: Slanting due to laser power (dashes signify 1 standard deviation).

Discussion

For both cross formation and slanting, the designed thickness of the wall did not have a significant impact. This is likely due to the two defect types being in perpendicular directions to the thickness. This parameter was varied to determine if the depth of each face had an impact on the formation of their corresponding defects. However, the results clearly show that is not the case. There were no significant differences between the 0.38- and 0.50-mm samples. Additionally, while there was a greater difference between the thin-wall transition thickness of 1.00 mm and the other two samples, none of the results were statistically significant. Therefore, the impact of thickness on cross formation and slanting are negligible within the thin wall regime.

In contrast, SAR had an impact on both cross formation and slanting. Samples with higher SAR had higher cross formation but less slanting. Meanwhile, samples with lower SAR had lower cross formation but more slanting. This matches results from prior literature. The greater length of the slits in the horizontal direction led to a longer overhang, which has been shown to be more likely to form cross. The longer the unsupported overhang,

the more likely dross will form. Due to the small size of these components, they are not conducive to support structures or post-process machining, meaning that the surfaces cannot be supported underneath or cleaned after manufacturing. Additionally, the longer height of the slits made the slits more susceptible to deformation due to pressure from the recoater blade. However, one observation to note is while the sides of the slits were slanting, the sides of the whole wall were still less susceptible to such slanting, and even when the slanting existed, it was limited to heights where slits were present. This implies that these defects are unlikely to impact other sections of the same part down the recoat direction.

Finally, laser power had smaller impact on both dross formation and even less on slanting. Contrary to prior literature, increasing power resulted in less dross formation. However, there is a reasonable explanation. The dross formation in these walls was due more to LoF than the traditional deeper melt pool seen in overhang literature. Since the thin walls were already more susceptible to LoF defects, increasing the laser power brought the wall out of the LoF regime but not into the keyholing regime. The lower laser powers led to less solid walls, so the top boundaries of the slits are collapsing instead of the melt pool dipping below the desired surface. If the power were to continue to increase further, keyholing-based dross formation would likely occur. However, with the current system, the laser power required to reach that condition would exceed the power limitation of 370 W and would need to be studied in future work. This impact is more obvious when evaluating the impact of power of different SAR values. While the samples with higher SAR had significant dross formation regardless of power, the samples with smaller SAR saw less dross formation as power increased. This impact was less prevalent in the slanting, as power did not have major impact. However, this is likely due to the significant dross formation, especially in the samples with higher SAR. When the dross formation is severe enough, the boundary between the top and sides of the slits becomes less clear, meaning that measuring the slanting becomes more difficult. Future work can explore how the keyholing regime impacts this behavior.

Conclusions

In this work, the impact of three parameters (wall thickness, slit aspect ratio, and laser power) were studied for their impact on printing slitted thin walls in laser powder bed fusion. Thin walls were printed with varying combinations of each parameter to understand how they behave individually and together by measuring dross formation on the top surface and the slanting of the side surfaces of the wall slits. While the wall thickness did not have significant impact on either dross formation or slanting, slit aspect ratio and laser power both had significant impact. Future work can explore how these design features interact with other features and how additional machine parameters impact this interaction. This information will allow designers to have more freedom to accurately design components to have the features they desire, using metal additive manufacturing to its full potential.

Acknowledgements

The authors would like to thank Los Alamos National Laboratory for providing funding for this work.

References

- [1] B. Blakey-Milner *et al.*, “Metal additive manufacturing in aerospace: A review,” *Mater. Des.*, vol. 209, p. 110008, 2021, doi: 10.1016/j.matdes.2021.110008.
- [2] Z. Wu, S. P. Narra, and A. Rollett, “Exploring the fabrication limits of thin-wall structures in a laser powder bed fusion process,” *Int. J. Adv. Manuf. Technol.*, vol. 110, no. 1–2, pp. 191–207, 2020, doi: 10.1007/s00170-020-05827-4.
- [3] A. J. Dunbar, G. J. Gunderman, M. C. Mader, and E. W. Reutzler, “Fabrication and quality assessment of thin fins built using metal powder bed fusion additive manufacturing,” *Solid Free. Fabr. 2017 Proc. 28th Annu. Int. Solid Free. Fabr. Symp. - An Addit. Manuf. Conf. SFF 2017*, pp. 2650–2663, 2017.
- [4] J. Kranz, D. Herzog, and C. Emmelmann, “Design guidelines for laser additive manufacturing of lightweight structures in TiAl6V4,” *J. Laser Appl.*, vol. 27, no. S1, 2015, doi: 10.2351/1.4885235.
- [5] A. Chakraborty *et al.*, “In-process failure analysis of thin-wall structures made by laser powder bed

- fusion additive manufacturing,” *J. Mater. Sci. Technol.*, vol. 98, pp. 233–243, 2022, doi: 10.1016/j.jmst.2021.05.017.
- [6] A. Gaikwad, F. Imani, P. Rao, H. Yang, and E. W. Reutzel, “Design Rules and In-Situ Quality Monitoring of Thin-Wall Features Made Using Laser Powder Bed Fusion,” in *Manufacturing Science and Engineering Conference*, 2019, pp. 1–20.
- [7] H. Yang, J. Yang, W. Huang, Z. Wang, and X. Zeng, “The printability, microstructure, crystallographic features and microhardness of selective laser melted Inconel 718 thin wall,” *Mater. Des.*, vol. 156, pp. 407–418, 2018, doi: 10.1016/j.matdes.2018.07.007.
- [8] P. Gradl, A. Cervone, and P. Colonna, “Influence of build angles on thin-wall geometry and surface texture in laser powder directed energy deposition,” *Mater. Des.*, vol. 234, no. September, p. 112352, 2023, doi: 10.1016/j.matdes.2023.112352.
- [9] M. Shange, I. Yadroitsava, A. Du Plessis, and I. Yadroitsev, “Roughness and Near-Surface Porosity of Unsupported Overhangs Produced by High-Speed Laser Powder Bed Fusion,” *3D Print. Addit. Manuf.*, vol. 9, no. 4, pp. 288–300, 2022, doi: 10.1089/3dp.2020.0097.
- [10] P. Lin, M. Wang, V. A. Trofimov, Y. Yang, and C. Song, “Research on the Warping and Dross Formation of an Overhang Structure Manufactured by Laser Powder Bed Fusion,” *Appl. Sci.*, vol. 13, no. 6, 2023, doi: 10.3390/app13063460.
- [11] T. Yang *et al.*, “Effect of processing parameters on overhanging surface roughness during laser powder bed fusion of AlSi10Mg,” *J. Manuf. Process.*, vol. 61, no. June 2020, pp. 440–453, 2021, doi: 10.1016/j.jmapro.2020.11.030.
- [12] S. C. Subedi, A. Shahba, M. Thevamaran, D. J. Thoma, and K. Suresh, “Towards the optimal design of support structures for laser powder bed fusion-based metal additive manufacturing via thermal equivalent static loads,” *Addit. Manuf.*, vol. 57, no. December 2021, p. 102956, 2022, doi: 10.1016/j.addma.2022.102956.
- [13] “ISO_25178-2-2012_Surf Text-Areal-Terms, Defn, Params.”